Ballistic Brownian Motion of Nanoconfined DNA

Ignacio Madrid, Zhiyong Zheng, Cedric Gerbelot, Akira Fujiwara, Shuo Li, Simon Grall, Katsuhiko Nishiguchi, Soo Hyeon Kim, Arnaud Chovin, Christophe Demaille, et al.

Ballistic Brownian Motion of Nanoconfined DNA

Ignacio Madrid[1λ], *Zhiyong Zheng*[2λ], *Cedric Gerbelot*[3λ], *Akira Fujiwara*[3*], *Shuo Li*[1], *Simon Grall*[1], *Katsuhiko Nishiguchi*[3], *Soo-Hyeon Kim*[1], *Arnaud Chovin*[2], *Christophe Demaille*[2]*, and *Nicolas Clement*[1,3]*

[1] IIS, LIMMS CNRS-IIS UMI2820, The Univ. of Tokyo; 4-6-1 Komaba, Meguro-ku Tokyo, 153-8505, Japan

[2] Laboratoire d'Electrochimie Moléculaire, UMR 7591 CNRS, Université Paris Cité, 15 rue Jean-Antoine de Baïf, F-75205 Cedex 13, Paris, France

[3] NTT Basic Research Laboratories, NTT Corporation, 3-1, Morinosato-Wakamiya, Atsugi-shi, 243-0198, Japan

Corresponding Author

Akira Fujiwara: akira.fujiwara.kd@hco.ntt.co.jp

Christophe Demaille: christophe.demaille@univ-paris-diderot.fr

Nicolas Clement: nclement@iis.u-tokyo.ac.jp

KEYWORDS: DNA, Brownian motion, ballistic motion, nanoconfinement, molecular dynamics, nanoelectrochemistry, nanogap

ABSTRACT: Theoretical treatments of polymer dynamics in liquid generally start with the basic assumption that motion at the smallest scale is heavily overdamped; therefore, inertia can be neglected. We report on the Brownian motion of tethered DNA under nanoconfinement, which was analyzed by molecular dynamics simulation and nanoelectrochemistry-based single-electron shuttle experiments. Our results show a transition into the ballistic Brownian motion regime for short DNA in sub-5-nm gaps, with quality coefficients as high as 2 for double-stranded DNA, an effect mainly attributed to a drastic increase in stiffness. The possibility for DNA to enter the underdamped regime could have profound implications on our understanding of the energetics of biomolecular engines such as the replication machinery, which operates in nanocavities of a few nanometers wide.

The recent experimental observations of ballistic Brownian motion[1,2] or resonances arising from hydrodynamics memory[3] for micrometric beads in optical trap experiments have confirmed that their time-dependent mean squared deviations can be completely different from those predicted by Einstein's theory of Brownian motion in a diffusive regime.[1,4] Moreover, the thermal forces can have a colored, that is nonwhite, noise spectrum.[3,5] Deviations from the standard diffusive regime also have been observed in single-protein electron transfer experiments with subdiffusion;[6] this motion can be described well by a generalized Langevin equation with fractional Gaussian noise.[7] However, behavior similar to ballistic Brownian motion is unexpected for polymers such as DNA in liquid due to their small mass and stiffness,[8] which leads to the common assumptions that the motion is heavily overdamped and therefore inertia can be neglected.[8–11] This excludes motions on 1-2 Angstrom distances[12] or ultrafast experiments using extremely short photoexcitation pulses

that can unveil the intrinsic nature of protein elementary motions before thermally activated processes start to play a role.[13,14]

Among the wide variety of polymers, DNA is of particular interest for the investigation of Brownian motion at a short time scale because its stiffness and dynamics have been widely studied by using fluorescence resonance energy transfer, atomic force microscopy, and micro / nanofluidic experiments.[15–18] Coarse-grained molecular dynamics (MD) DNA models such as OxDNA[19] additionally provide a good description of the elastic properties of single and double-stranded DNA (ssDNA and dsDNA, respectively), including not only the persistence length and torsional modulus, but also nontrivial features such as twist-bend coupling.[20] However, the motional dynamics of short, end-tethered DNA is still the subject of great controversies. For example, the electrochemistry community, which uses a redox marker such as ferrocene (Fc) at the extremity of DNA (for sensing applications), typically reports abnormally slow DNA motion that is orders of magnitude lower than expected.[21–24] In contrast, fluorescence quenching experiments, performed with similar tethered DNA, marked with a fluorophore, suggest that the dynamics of end-anchored DNA is that expected from Brownian motion.[9]

Vertical nanoconfinement provides an additional degree of freedom for tuning DNA stiffness and Brownian motion time constants. Nanofluidic experiments in ~60-nm channels on long DNA have shown that the normalized DNA spring constant, βk_c, scales as z_{gap}^{-2}, where $\beta=(k_BT)^{-1}$ is the inverse of thermal energy and z_{gap} is the channel width.[25] This z_{gap} dependence can be derived from the Odijk polymer model.[25] Therefore, an increase of βk_c by up to two orders of magnitude is expected with further scaling of the channel to only a few nanometers. Such a regime has been insufficiently explored due to experimental and related data analysis challenges. Nevertheless, it is extremely important to investigate this type of structure to confirm such a possibility to tune the DNA spring

constant under nanoconfinement and, more generally, to understand the Brownian motion of polymers under nanoconfinement, due to its similarity with biological systems featuring nanocavities of a few nanometers in width (*e.g.*, the replication machinery).

Herein, we report on the Brownian motion of the free extremity of short, end-tethered, and nanoconfined ssDNA and dsDNA, which were studied using MD simulations and nanoelectrochemistry-based single-electron-shuttle experiments. Our MD results confirmed a drastic increase in the DNA spring constant under nanoconfinement, unlocking the ballistic Brownian motion regime. The experimental nanoelectrochemical study indicates that electron transfer at electrode interfaces governs the charge current as opposed to an apparently slow diffusion-limited process. A simple analytical model for the electrochemical current is introduced and used to evidence the inertial motion, which is also validated by a "digital experiment" combining MD and single-electron counting. The quality coefficient Q of DNA spring under nanoconfinement is extracted and discussed.

RESULTS AND DISCUSSION

Molecular Dynamics Simulation of End-Tethered DNA Under Nanoconfinement

The system considered first is a ~10-nm-long 20-mer oligonucleotide (both ssDNA dT_{20} and fully hybridized dsDNA $(dT.dA)_{20}$) attached by one of its extremities to an anchoring (bottom) plate and confined by an incoming (top) plate. The plates formed a planar nanogap of width z_{gap}, containing a high-salt aqueous solution (Figure 1a).

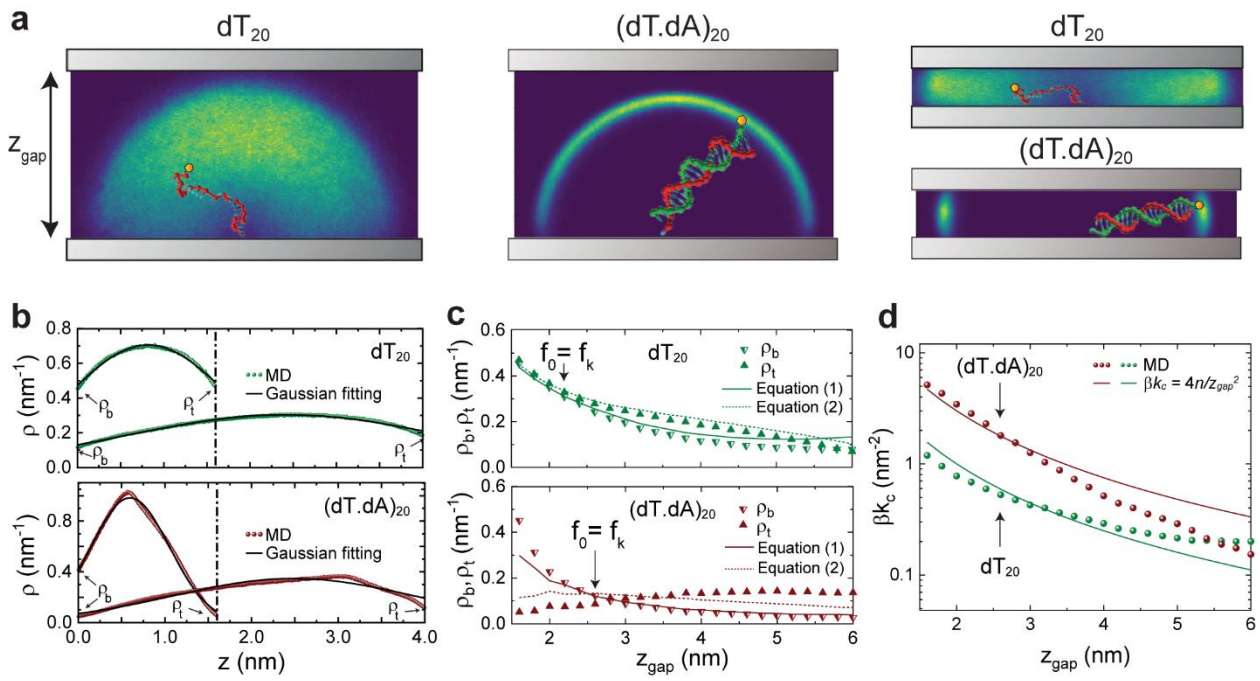

Figure 1. MD analysis of end-grafted DNA confined in a nanogap. Spatial distribution of the position of the DNA free end. (a) Schematic representation of the device composed of a 20-mer oligonucleotide (dT_{20} for ssDNA, or $(dT.dA)_{20}$ for dsDNA) end-attached to a bottom plate and confined to a gap of width z_{gap} by an upper plate. The free extremity of the DNA is represented by an orange dot. Heat maps representing the distribution of the position of the DNA free end in a vertical slice of space perpendicular to the plates are shown, both without (left, z_{gap} = 8 nm) and with (right, z_{gap} = 2.4 nm) nanoconfinement. (b) Probability density, ρ, of finding the free end of the DNA at a distance z above the bottom plate at z_{gap} = 1.5 nm and z_{gap} = 4 nm, respectively. (c) Probability of finding the DNA free end at the bottom plate, ρ_b, or at the top plate, ρ_t, vs. z_{gap}. (d) DNA spring constant, βk_c, obtained from Gaussian fits of the $\rho - z$ distributions, vs. z_{gap}. Solid lines are $\beta k_c = 4n/z_{gap}^2$ with n = 1, 3 for ssDNA and dsDNA, respectively.

We studied this system by MD using OxDNA code (Figure S1-2; see Methods). The model incorporates various interactions that occur between adjacent nucleotides, including base stacking,

hydrogen bonding, excluded volume, and electrostatic interactions. These interactions have been fine-tuned to accurately reproduce the structure, thermodynamics,[26] and mechanical properties of single and double-stranded DNA. The electrostatic potential of the model follows the Debye-Huckel form, with adjustments made to account for the impact of $[Na^+]$ on hybridization thermodynamics. The simulations described in this work were conducted under experimental conditions of $[Na^+]$ = 1 M. The most recent version of the model incorporates base-specific strengths for stacking and hydrogen-bonding interactions. We tracked the position of the free end of the DNA strand. Two-dimensional heat maps representing the distribution of this position in a vertical slice of space perpendicular to the plates are shown in Figure 1a, for both dT_{20} and $(dT.dA)_{20}$, with and without nanoconfinement. The MD simulations of unconfined DNA showed the expected "mushroom" distribution for flexible ssDNA[27] and a hemispherical distribution for rigid dsDNA due to rotational diffusion around its anchored extremity.[9,21] We focused specifically on the equilibrium distribution of the free end position of the DNA along the z-axis. Figure 1b shows the probability density, ρ, of the presence of the DNA free extremity vs. z, for gaps of 1.5 nm and 4 nm wide. Figure 1c shows ρ at the bottom and top interfaces (ρ_b and ρ_t, respectively) that are important variables for the experimental analysis. We noted an asymmetry at these interfaces, which varied with z_{gap}. This effect can be quantitatively analyzed, as described below. $\rho - z$ can be fitted reasonably well by a Gaussian distribution for all gaps (Figure 1b). The DNA spring constant, βk_c, can thus be assessed from the variance of the ρ distribution, Equation (5). Our MD simulations confirmed that βk_c scales as z_{gap}^{-2} even down to z_{gap} = 1.5 nm (Figure 1d), following Odijk's spring constant model under vertical nanoconfinement, as previously reported for 60 nm gaps.[25] For the short and tethered DNA used here, the βk_c vs. z dependence shown in Figure 1d can be quantitatively described by the equation: $\frac{1}{2}\beta k_c(z_{gap}/2)^2 = n/2$; where n = 1 for

ssDNA and $n = 3$ for dsDNA. The larger n value for dsDNA could be related to the number of degrees of freedom (*e.g.*, associated with a rotational diffusion).[9,21] A similar behavior of βk_c is found for a longer chain length (dT_{35}; see Figure S3). To put these numbers in perspective, the value of $k_c \sim 1.2 \times 10^4$ μN m^{-1} found for $(dT.dA)_{20}$ and $z_{gap} = 2$ nm, is equivalent to the spring constant of a soft cantilever used to image biological materials by atomic force microscopy. It is also much larger than k_c values achieved in optical trap experiments (Table S1), favoring the observation of ballistic Brownian motion even when the mass is extremely small, as described below.

In order to understand the impact of such a large DNA stiffness on the Brownian motion under confinement, we analyzed the power spectral density of the z position of the DNA free end vs. time (S_z). Similar to the optical spectrum of an atom, it provides valuable information on the system, including time constants and the nature of the motion.[3,4] Two contributions can be identified (Figure 2a for dT_{20} at $z_{gap} = 2.2$ nm; see Figure S5 for other z_{gap} and $(dT.dA)_{20}$, Figure S6 with Supporting Discussion 2 for details and Equation (S1)). The first one is related to the Brownian motion of a trapped particle in a harmonic potential with inertia.[4] This contribution is identical to the trapped microspheres in optical traps, featuring a f^{-4} dependence at high frequency. The second one, with a f^{-2} slope after the f^{-4} slope, is specific to the system under study. We show, using a numerical approach based on Kramers equation,[28] that it is due to the reflective boundaries (see Figure S4 and Supporting Discussion 1). Considering the quality coefficient Q shown in Figure 2b provides reasonable fits to S_z for different z_{gap} (Figure S5). The natural angular frequency is $f_0 = (1/2\pi)\sqrt{k_c/m^*}$ with m^* the effective DNA mass. m^* values obtained from f_0 and k_c (Table S1), are in the range of expectations for the physical DNA mass m, in particular for dsDNA. At small z_{gap} (*e.g.*, $z_{gap} = 1.6$ nm, Figure 2b, inset), Q is unambiguously obtained from the resonance

peaks, which are signatures of the ballistic Brownian motion of the DNA. The only difference is a peak splitting observed for dsDNA (Figure 2b, inset) that we attribute to a strong coupling between the vibration modes of complementary bases and the resonant frequency of the confined dsDNA (see Figure S6 and Supporting Discussion 2). Interestingly, Q at small gaps in Figure 2b is similar to values found in previous ballistic Brownian motion studies with micrometric beads[1,2] (Table S1).

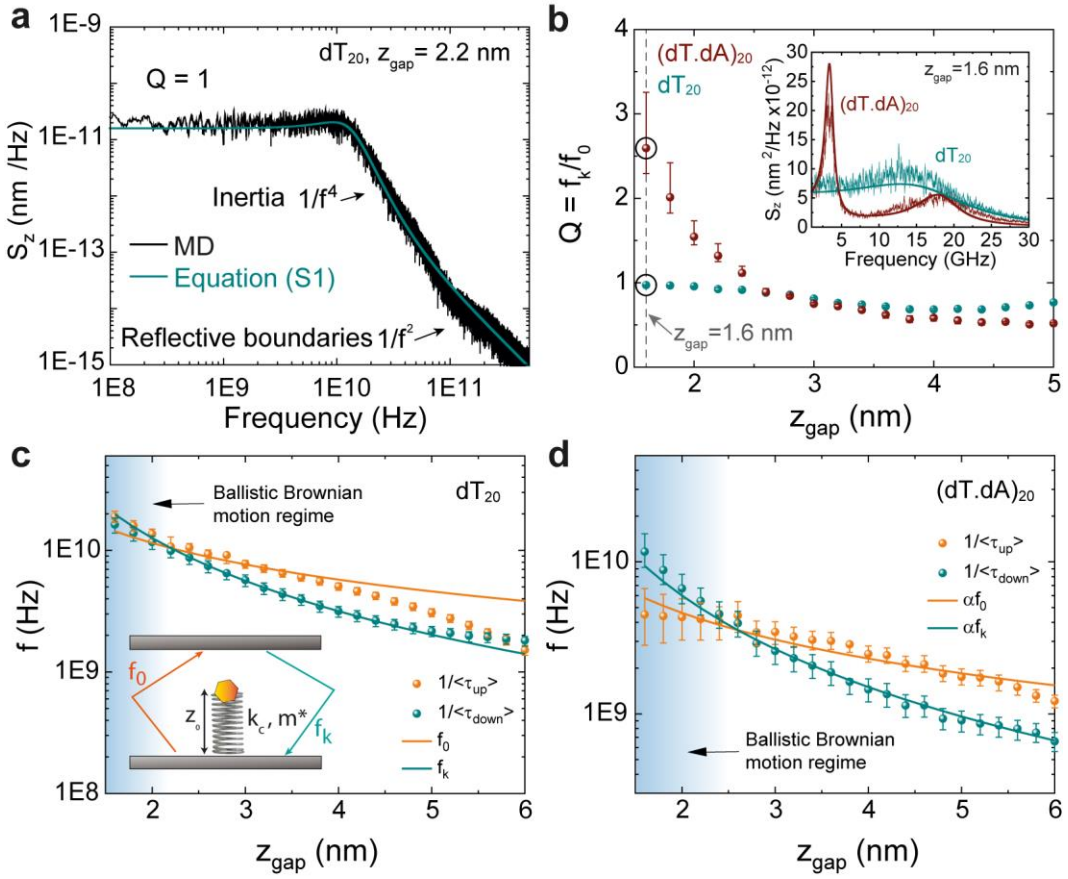

Figure 2. Evidence of the inertia effect from power spectral density analysis of z position of the DNA free end vs. time (S_z) from MD time tracks of 20-mer DNA. (a) Example of S_z for dT_{20} and z_{gap} = 2.2 nm. Equation (S1) is used for the analytical model (solid line), with $Q = 1$, $f_0 = f_k = 1.32 \times 10^{10}$ Hz, $\beta k_c = 0.82$ nm^{-2}, $D = 0.7 \times 10^9$ nm^2·s^{-1}. (b) Quality coefficient Q used in the analytical

model (Equation (S1)) to reproduce S_z data, (Figure S5, S8, and Supporting Discussion 4 example at different z_{gap}), with $Q = f_k/f_0$ taken from Figure 2c and d, including error bars. Inset: PSD at z_{gap} = 1.6 nm for dT_{20} and $(dT.dA)_{20}$ with solid lines from Equation (S1) considering Q from this figure. The peak splitting details are available in Figure S6 and Supporting Discussion 2. (c) $<\tau_{up}>^{-1}$ and $<\tau_{down}>^{-1}$ as a function of z_{gap} obtained from dT_{20} MD tracks with a threshold $\varepsilon = 0.3 \pm 0.1$ nm that determines error bars (see Figure S7 and Supporting Discussion 3). $f_0 = (1/2\pi)\sqrt{k_c/m^*}$ with k_c shown in Figure 1d and dT_{20} mass $m^* = 0.07m$ (Table S1) and $f_k = Qf_0$ are shown for comparison. Inset: Schematic illustration of f_k and f_0 assuming DNA as a compressed spring. (d) $<\tau_{up}>^{-1}$ and $<\tau_{down}>^{-1}$ as a function of z_{gap} obtained from $(dT.dA)_{20}$ MD tracks with a threshold $\varepsilon = 0.3 \pm 0.1$ nm that determines error bars. αf_k and αf_0 for $(dT.dA)_{20}$ with $\alpha = 1.4$ and $(dT.dA)_{20}$ mass $m^* = 1.3m$. (Table S1). α slightly different from unity comes from the arbitrary nature of ε.

Further analysis of the time constants (Figure 2c, d) revealed that the average first passage time $<\tau_{up}>$ from the bottom plate to the top plate (see details in Figure S7) can be well described by $f_0 \approx <\tau_{up}>^{-1}$. Similarly, the average first passage time $<\tau_{down}>$ from the top plate to the bottom plate can be well described by $f_k \approx <\tau_{down}>^{-1}$ with $f_k = Qf_0$. In other words, the upward motion can be described by an inertial motion (corresponding to an initially strongly compressed spring), whereas the downward rate is well described by a diffusive motion with the usual escape rate ~ k/γ of a confined particle in a harmonic trap (Figure 2c, inset), with γ the Stokes friction coefficient. We can write (see Figure S7 for details):

$$\rho_b = \rho_s \times 2<\tau_{down}> / (<\tau_{up}> + <\tau_{down}>) \approx 2\rho_s / [(1 + Q^{-1})] \quad (1)$$

$$\rho_t = \rho_s \times 2<\tau_{up}> / (<\tau_{up}> + <\tau_{down}>) \approx 2\rho_s / [(1 + Q)] \quad (2)$$

where ρ_s [nm^{-1}] corresponds to the probability of finding the DNA free end at the bottom and top interfaces in the case of a symmetric motion ($<\tau_{up}> = <\tau_{down}>$), which is obtained when $Q = 1$. ρ_s can be derived analytically (Equation (6) – (9)) and depends on βk_c; $\rho_s = 0.71/z_{gap}$ for dT_{20} and $\rho_s = 0.33/z_{gap}$ for $(dT.dA)_{20}$. Equations (6) and (7) then enable the simulated ρ_b and ρ_t vs. z_{gap} variations shown in Figure 1c to be nicely reproduced (using the Q vs. z_{gap} data shown in Figure 2b). It is worth noting that $<\tau_{up}>$ and $<\tau_{down}>$ are extremely fast, in the sub-nanosecond range.

Single-electron Shuttle Experiment

Nanoelectrochemistry, in which the confining plates are independently biased electrodes (a microelectrode "tip" and a flat DNA-tethering "bottom" gold surface), is a powerful way to confirm experimentally MD predictions. In such experiments,[11,29] the molecular motion of the DNA strand brings a Fc label attached to its free end alternatively in contact with both electrodes (Figure 3a). Fc is oxidized to Fc^+ upon contact with the upper electrode, while Fc^+ is reduced back to Fc at the bottom electrode. This redox cycling generates a stationary electrochemical current, I, through the electrodes. This approach is extremely attractive for the following reasons: First, at a high ionic strength (1 M) and room temperature, the potential drops within the first few angstroms of each electrode. Therefore, DNA motion is not affected by electrode bias.[9] Second, Fc is a 3-Å-diameter redox label, which can either be in its reduced (Fc) or oxidized (Fc^+) state; thus, it behaves as a single-electron box. It is small enough not to affect the motion of DNA. The charge state of Fc is also expected not to affect the DNA motion at a high ionic strength. Third, as the electron transfer rate at electrodes k_V is much slower than Fc's motion between the two electrodes ($k_V << min(<\tau_{up}>^{-1}, <\tau_{down}>^{-1})$) with a symmetric electron transfer rate k_V at top and bottom electrode, and as the probability of electron transfer to Fc decreases exponentially with z with a decay ratio β_d of

1 Å^{-1} (Equation (12) – (14)), the electron-transfer-limited current I can be related to ρ_t and ρ_b (from Equation (1), (2) and Equation (15)):

$$I = Ne\frac{k_V}{\beta_d}\frac{\rho_t\rho_b}{(\rho_t+\rho_b)} \approx Ne\frac{k_V}{\beta_d}\frac{\rho_s}{\left[1+\frac{1}{2}\left(\frac{1}{Q}+Q\right)\right]} \quad (3)$$

where N is the number of molecules addressed by the tip and e is the elementary charge. In other words, this newly introduced Equation (3) suggests that Q can be extracted from DC current measurements without the need for ultra-high speed (picosecond range) and Å-precision label tracking, which would be extremely challenging experimentally. An analogy can be made with the recent understanding of picosecond coherent electron motion in a silicon single-electron source achieved from DC current measurements.[30] Fourth, master equations describing the z-dependent probabilities of electron transfer can be computed every picosecond on the MD track to generate every single-electron transfer leading to a "numerical electrochemical experiment" based on MD (Equation (12) and (13), Figure 3a). We introduce here a code (Q-biol, see Methods) freely available[31] based on MD coupled with single-electron counting. It has been optimized for such a configuration with long MD tracks and is able to reproduce numerically the experiments. It also includes resonant tunneling effect (see Methods).

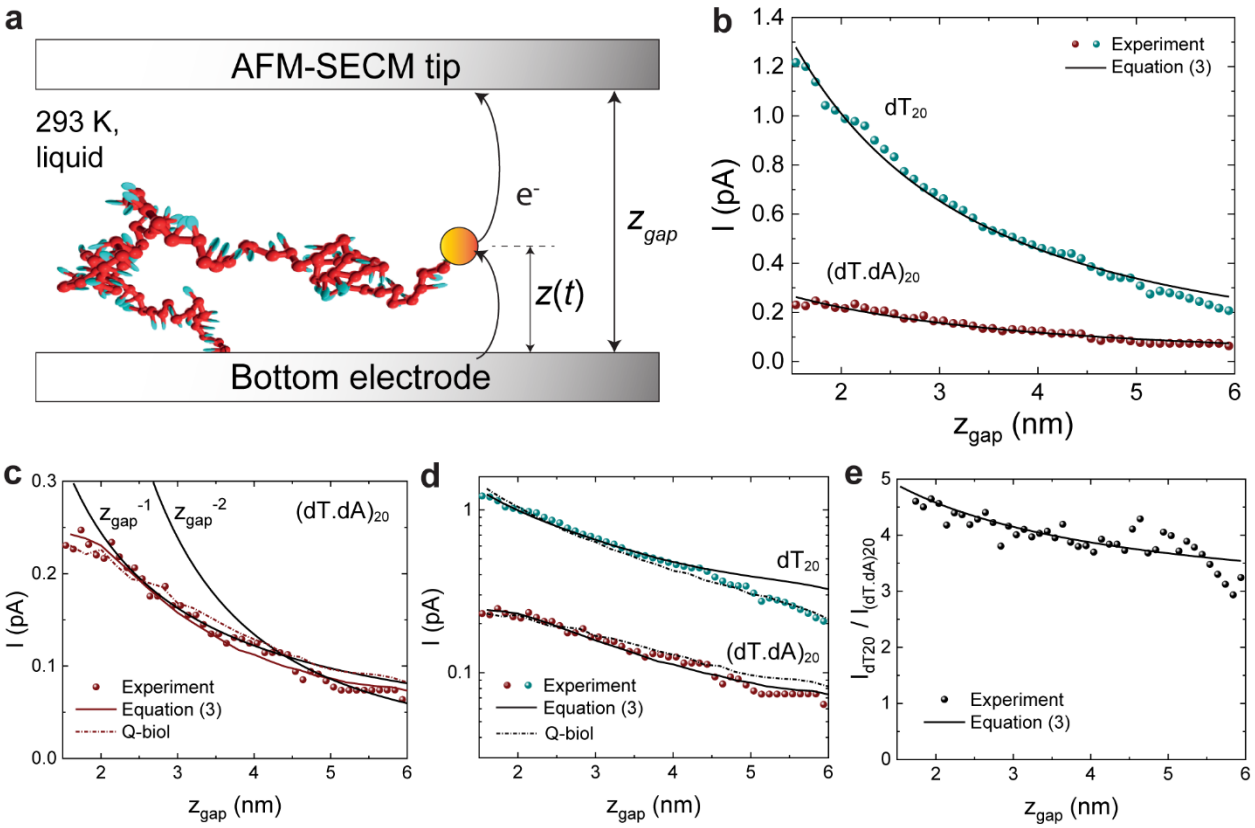

Figure 3. Evidence of the inertia effect from nanoelectrochemical experimental and numerical measurements. (a) Schematic representation of the system under study composed of a top electrode (which is experimentally the tip of an AFM-SECM) and a gold bottom electrode tethered ssDNA or dsDNA with an Fc redox label at the free end. $z(t)$ and z_{gap} are defined graphically. Electrons are transferred one by one from the bottom electrode to the top electrode via Fc. (b) Experimental measurements of the electrochemical current generated by the system described in (a) from ref,[11] as probed by AFM-SECM in molecule touching mode. Fits with Equation (3) give $k_V = 3.56 \times 10^8$ s^{-1}, $\Theta = 2.12$ for dT_{20} and $k_V = 1.8 \times 10^8$ s^{-1}, $\Theta = 3.47$ for $(dT.dA)_{20}$. The bottom and top electrodes are biased at -0.25 V vs. Fc/Fc^+ and +0.1 V vs. Fc/Fc^+, respectively, large enough biases to be in the Marcus rate saturation in this system (Equation (14) and Figure S13). Data are provided for both dT_{20} and $(dT.dA)_{20}$. (c) Detailed analysis of the approach curve for $(dT.dA)_{20}$. Numerical

simulation of the electrochemical current generated for $(dT.dA)_{20}$ with Equation (3) (parameters shown above) and with Q-biol (digital experiment with single-electron counting, see Methods). In Q-biol (Equation (12), (13)), $k_V = 3.09\times10^8\ s^{-1}$ for dT_{20} and $k_V = 1.64\times10^8\ s^{-1}$ for $(dT.dA)_{20}$. (d) Log scale representation of the approach curves with detailed analysis for dT_{20} and $(dT.dA)_{20}$. (e) Ratio of the dT_{20} to $(dT.dA)_{20}$ currents vs. z_{gap} as derived from the experimental approach curves in (b) or calculated from Equation (3).

The related experiments were performed using atomic force microscopy–scanning electrochemical microscopy in molecule touching mode, AFM-SECM[11] at fixed bias while varying the tip-surface distance, z_{gap} (Figure 3a, see Methods). The top and the bottom electrodes were biased at potentials respectively positive and negative enough vs. Fc/Fc^+, the standard potential of the Fc head, for the current not to depend on their exact values. In this situation, the Marcus rate saturation regime is reached,[32] so that k_V is the same at both electrodes (Figure S13). The z_{gap} value was precisely calibrated from force–distance curves (see Figure S11). As a first set of experiments, we start by considering a set of I vs. z_{gap} approach curves recorded for 20-mer DNA (ssDNA dT_{20} and dsDNA $(dT.dA)_{20}$) that were previously published,[11] but not quantitatively exploited by lack of suitable model (Figure 3b). We propose to interpret these data based on the newly introduced Equation (3) and also compare them with the "digital experiment" based on single-electron counting (Q-biol). As a first analysis, experimental curves can be fitted with Equation (3) assuming $Q = \Theta / z_{gap}$ and $N = 1$, yielding best-fit values (calculated over 3 sets of experimental approach curves): $k_V = (4 \pm 1) \times 10^8\ s^{-1}$; $\Theta = 2.1 \pm 0.5$ and $k_V = (2.0 \pm 0.5) \times 10^8\ s^{-1}$; $\Theta = 3.5 \pm 0.5$, for dT_{20} and $(dT.dA)_{20}$, respectively (Figure 3b). Θ nicely compares with values derived from MD (from analytical models of f_0, f_k in Figure 2c, d) that provided $\Theta = 2.2$ and 2.6 for dT_{20} and $(dT.dA)_{20}$ respectively. Taking numerical values of Q from Figure 2b leads to an even better fit for $(dT.dA)_{20}$ as the rapid increase

of Q then accounts for the saturation of I at small gaps (Figure 3c). Conversely, too simple models solely based on electron transfer limited current (αz_{gap}^{-1}) or diffusion-limited current (αz_{gap}^{-2}) are not satisfactory at small z_{gap} (Figure 3c). Furthermore, the "digital experiment" with Q-biol also confirms the validity of Equation (3) (Figure 3c, d). The difference in current between dT_{20} and $(dT.dA)_{20}$ (Figure 3d and e) can be simply and quantitatively explained by a larger ρ_s (lower k_c), lower Q values at small z_{gap} and higher k_V for dT_{20} and $(dT.dA)_{20}$ respectively, each effect contributing on a similar basis. The lower k_V for $(dT.dA)_{20}$ (~factor 2) compared to dT_{20} could be attributed to the reduced degrees of freedom of Fc facing the bottom electrode due to the rigidity of $(dT.dA)_{20}$, which can affect the electronic coupling parameter distribution between Fc and the electrode[33] (see Supporting Discussion 6 related to k_V in Figure S12, S13). Finally, an interesting observation from Equation (3) can be made at large enough z_{gap}, when $Q << 1$. Considering an electron transfer frequency $f_e = k_V \rho_s / \beta_d$, Equation (3) can be simplified to:

$$I = 2ef_k \frac{f_e}{f_0} \approx e \frac{f_e}{f_0} \frac{D}{z_{gap}^2} = e \frac{D^*}{z_{gap}^2} \qquad (4)$$

with $D^* = \frac{f_e}{f_0} D$. D^* can be seen as an effective diffusion coefficient. This demonstrates that, albeit controlled by the electron transfer rate, the current generated by the DNA motion in nanogaps can formally appear as being diffusion limited. D^* could match quantitatively with the apparent, about 3 orders of magnitude, slow diffusion reported.[22] A f_e/f_0 ratio may be important for Ballistic Brownian motion studies to confirm that the measurement does not affect the system under study due to the equipartition theorem.

Several assumptions in this study require discussion. Firstly, the neglected influence of electrode bias-related electrostatics on DNA motion needs to be addressed. At 1 M ionic strength, the Debye screening length in water at room temperature is approximately $\lambda_D \sim 3$Å. While small, this value

is not negligible when compared to the smallest z_{gap} of 1.5 nm. However, considering the electrostatics in nanoconfined systems is a nontrivial task that resides at the forefront of current knowledge. For instance, in nanogaps, the dielectric constant of water is expected to be significantly reduced,[34,35] further decreasing λ_D. Moreover, the molecular electronics community has studied such electrostatics effects in a nanogap and demonstrated a non-linear potential drop with a sharper decline at the interfaces.[36–38] Therefore, the operation at high-ionic strength has been considered in this study as a good trade-off to avoid considering such complex effects and to minimize the introduction of external energy into the system being studied. Although the 1 M operation deviates from the typical 0.1 M ionic strength found in biological systems, the fundamental comprehension of the inertia effects under strong confinement should remain applicable.

A second aspect is the lack of consideration of hydrodynamic effects in the MD simulation. While we expect these effects to be inhibited for nanometer-wide objects when compared to micrometric beads,[3] there have recently been some efforts to implement hydrodynamic collective effects,[39] but not implemented in OxDNA MD code due to the large impact on computation time.

Finally, the model described above for Q assumes liquid damping as the sole source of loss, which is a reasonable approximation for short DNA strands of 20-mer. However, other sources of loss may come into play, with the most relevant being thermomechanical loss, typically considered in the nanoelectromechanical systems community.[40,41] This additional loss would become more prominent with longer DNA strands due to changes in thermal conductivity.[40,42,43] It is expected to be primarily observed at small z_{gap} distances (Equation S7, see Supported Discussion 7). Importantly, Equation 3 remains valid and can still be utilized to determine Q. While a dedicated study specifically focused on length-dependent effects is beyond the scope of this paper, our

experiments on dT_{35} and $(dT.dA)_{35}$ suggest the presence of additional loss at small z_{gap} distances (Figure S14) that can be qualitatively explained by the thermomechanical loss. The analysis presented for dT_{20} and $(dT.dA)_{20}$ holds quantitatively true for dT_{35} and $(dT.dA)_{35}$, with similar values of (Θ, k_V), and a higher current for single-stranded DNA compared to double-stranded DNA (Figure S11).

Overall, an all-atom simulation that could reproduce the Stern layer at the gold interfaces including non-Coulombic ion-specific interactions,[44,45] hydrodynamic, electrostatic, and thermal dissipation effects would undoubtedly provide great insights into these inertial effects under nanoconfinement. It will however be extremely computing intensive as 10 µs of simulations are typically required to statistically describe the present system.

CONCLUSION AND OUTLOOK

In summary, the Brownian motion of tethered DNA under nanogaps was explored by MD simulation and nanoelectrochemistry-based single-electron shuttle measurements. A new formalism based on an electron-transfer limited current (Equation (3)) was introduced and used as a powerful way to extract Q from DC measurements. Q as large as 2-3 at the smallest z_{gap} have been extracted for dsDNA $(dT.dA)_{20}$, in good agreement with MD simulations and with the Q-biol code. Finally, this work shows that the Ballistic Brownian motion in polymers requires fine-tuning of the mass, confinement, and thermal conductivity to be observed.

This study established a direct link between molecular electronics,[46–49] biomechanics, and electrochemistry, highlighting the potential of nanoelectrochemical measurements to complement optical trap studies on Brownian motion at a short time scale. Future work will further exploit the potential of single-electron shuttle experiments by exploring theoretical (with Q-biol) and

experimental quantum shot noise measurements as a powerful way to assess asymmetry in the probability of presence,[50–52] but also to gain additional information on the motion at short time scale. Finally, the energetics of nanoconfined DNA (thermal conductivity and dissipation) will be explored. Inertia could be at the origin of the reduced DNA melting temperature reported under nanoconfinement,[53,54] which has for example been exploited to stabilize aptamers in their optimum configuration for cancer cell detection.[54] As the replication process, which operates in nanocavities of a few nanometers wide and about 14-17 bp opened loop,[55] is considered to be responsible for a substantial fraction of energy consumption in cells, *e.g.*, for prokaryotes, 13% of *Escherichia Coli* glucose consumption is channeled into making nucleotides,[56] inertia in nanoconfined biomolecules may have played an important role in the evolutionary development.[57]

METHODS

Information of the Coarse-Grained Model Using OxDNA and Post-Processing

The OxDNA model represents DNA at the nucleotide level in a simplified manner.[19,26,58,59] Each nucleotide is considered a rigid body with distinct sites for the backbone and base components (see Figure S1). The model incorporates various interactions that occur between adjacent nucleotides, including base stacking, hydrogen bonding, excluded volume, and electrostatic interactions.

Coarse-grained models of DNA provide several benefits when investigating mechanical properties. One advantage is the capability to execute simulations over sufficiently long timescales, as exemplified in this research, where simulations persisted for up to 10 μs. This feature is necessary to observe an adequate number of electron transfer events to generate *I-V* curves using the Q-biol code (refer to below).

Regarding the MD simulations utilizing the OxDNA model, multiple crucial parameters are implemented:

- A sharp transition is presumed at the boundaries between the plates and water, with repulsion planes exerting a force of 4.863 nN (equivalent to 100 OxDNA units).
- The attachment of the base at the 5' end to the surface involves a localized trap with an elastic force of 48.63 pN (10 OxDNA units).
- The base at the 3' end is monitored at an interval of 909 fs.
- The simulations are conducted at a temperature of 20 °C.
- A Langevin thermostat is utilized.

This study represents a highly specialized application of the OxDNA code. Several technical hurdles had to be addressed to accomplish the "DNA grafting" process. Specifically, this involved a multi-step procedure beginning with a Monte-Carlo simulation, followed by molecular dynamics simulations that gradually increased the punctual force up to 10 OxDNA units. Moreover, due to the temporal resolution of 909 fs over a 10 µs time scale, a custom Python code was developed to directly extract the position of the free end of the DNA. Furthermore, a RAMdisk was employed to mitigate potential errors arising from the large volume of data being written. The code also includes data analysis such as $\rho(z)$, βk_c, $<\tau_{up}>$, $<\tau_{down}>$, and slice heat maps as shown in Figure 1. In the case of dsDNA, we first check that the DNA is fully hybridized via the normalized value per base of the total hydrogen bond energy (Figure S2). For example, in the case where DNA would have been partly hybridized, a value < 0.15 eV would have been observed.

Analytical Model for the Density of Probability of the Presence of Fc

The probability density distribution function of the ferrocene (Fc) marker, ρ [nm^{-1}], can be obtained as a solution of the Fokker-Planck-Kolmogorov partial differential equation. Assuming a steady-state solution corresponding to very large times and post-relaxation of the DNA polymer, we get:

$$\rho(z) = \frac{\sqrt{\frac{2}{\pi}}\sqrt{\beta k_c}\, e^{-\frac{1}{2}(z-z_0)^2 \beta k_c}}{Erf\left[\frac{(z_{gap}-z_0)\sqrt{\beta k_c}}{\sqrt{2}}\right] + Erf\left[\frac{z_0\sqrt{\beta k_c}}{\sqrt{2}}\right]} \frac{1}{z_{gap}} \tag{5}$$

ρ is a Gaussian with mean z_0 and variance given by the inverse of the spring constant $1/\beta k_c$. z_0 is a variable associated with asymmetry (including inertia effects).

At $z = 0$:

$$\rho_b = \rho(0) = \frac{\sqrt{\frac{2}{\pi}}\sqrt{\beta k_c}\, e^{-\frac{1}{2}(z_0)^2 \beta k_c}}{Erf\left[\frac{(z_{gap}-z_0)\sqrt{\beta k_c}}{\sqrt{2}}\right] + Erf\left[\frac{z_0\sqrt{\beta k_c}}{\sqrt{2}}\right]} \frac{1}{z_{gap}} \tag{6}$$

At $z = z_{gap}$:

$$\rho_t = \rho(z_{gap}) = \frac{\sqrt{\frac{2}{\pi}}\sqrt{\beta k_c}\, e^{-\frac{1}{2}(z_{gap}-z_0)^2 \beta k_c}}{Erf\left[\frac{(z_{gap}-z_0)\sqrt{\beta k_c}}{\sqrt{2}}\right] + Erf\left[\frac{z_0\sqrt{\beta k_c}}{\sqrt{2}}\right]} \frac{1}{z_{gap}} \tag{7}$$

For dT_{20}, assuming $z_0 = z_{gap}/2$ and the Odik's spring constant, with $\beta k_c (z_{gap}/2)^2 = 1$, we get:

$$\rho_s = \rho_b = \rho_t = \frac{\sqrt{\frac{8}{\pi}}\, e^{-\frac{1}{2}}}{2Erf\left[1/\sqrt{2}\right]} \frac{1}{z_{gap}} \approx 0.71/z_{gap} \tag{8}$$

For $(dT.dA)_{20}$, assuming $z_0 = z_{gap}/2$ and Odik's spring constant, with $\beta k_c (z_{gap}/2)^2 = 3$, we get:

$$\rho_s = \rho_b = \rho_t = \frac{\sqrt{\frac{24}{\pi}}\, e^{-\frac{3}{2}}}{2Erf\left[\sqrt{3/2}\right]} \frac{1}{z_{gap}} \approx 0.33/z_{gap} \tag{9}$$

Analytical Model for S_z

The power spectrum of the Brownian motion for the free extremity of laterally confined DNA (and attached at the other extremity) should be similar to the optical spectrum of an atom or a trapped microsphere/particle in a harmonic potential. The power spectral density (PSD) of a variable is obtained by squaring the modulus of its Fourier transform. The Brownian motion of a particle in a harmonic trap, without boundary conditions (Ornstein-Uhlenbeck equation), has been studied analytically by Uhlenbeck and Ornstein,[60] and Wang and Uhlenbeck.[61] The PSD is:[4]

$$S_z(\omega) = \frac{2k_bT}{m^*{\omega_0}^2} \frac{{\omega_0}^2\Gamma_0}{({\omega_0}^2 - \omega^2)^2 + \omega^2{\Gamma_0}^2} \tag{10}$$

where k_b is the Boltzmann constant, T the temperature, m^* the (DNA effective) mass, $\omega_0 = (k_c/m^*)^{0.5}$ is the natural angular frequency (of the DNA free extremity) when there is no damping, and Γ_0 the damping coefficient. Considering $\beta = 1/(k_bT)$, $\Gamma_0 = \gamma/m^*$ where γ is the Stokes friction coefficient of Fc, $Q = (k_cm^*)^{0.5}/\gamma$, $\omega_k = Q\omega_0$, Equation (10) can be rewritten as:

$$S_z(f) = \frac{1}{\pi\beta k_c} \frac{Q^{-1}}{\left[\left(1 - \left(\frac{f}{f_0}\right)^2\right)^2 + \left(\frac{f}{f_k}\right)^2\right]} \tag{11}$$

f, f_0, and f_k are the frequencies related to pulsations ω, ω_0, and ω_k, respectively. In our specific case, taking into account that k_c can be explicitly written with z_{gap} and f_0, f_k are linked as $f_k = Qf_0$, there are only two variables in Equation (11). Equation (11) is valid for both underdamped and overdamped systems.[4] Equation (11) provides reasonable fits to our results, however it cannot reproduce the coexistence of f^4 and f^2 slopes as in Figure 2a. This can be understood by taking

into account boundaries (reflective walls). It requires numerical simulations described below. *Note that this effect of boundary walls is quite specific to the system under study as there were no boundaries in other studies of ballistic Brownian motion with optical traps.*

Q-biol Code (the "digital experiment" counting electrons)

The Q-biol code is intended to be used as a general quantum (bio)electrochemical software, or "numerical experiment", that will include free redox molecules, redox-labeled DNA of any sequence, or antibodies. This study is the first exploitation of Q-biol. Q-biol converts a Track file (*z*-*t*) (see MD methods section for this study) into an electrochemical current. Previous studies have reported a similar approach in one electrode configuration to reproduce cyclic voltammograms by counting electrons.[23,62] These studies have focused on the Brownian motion of freely moving molecules. For example, in ref,[23] the Brownian motion of a free molecule in a half-sphere of radius *R* has been considered to mimic the Brownian motion of DNA of length *R*. Here, we use MD to model DNA motion, a two-electrode configuration and implemented computation approaches enabling computation on long time frames (10 μs) in minutes. The computation efforts have been extremely important to allow low electron transfer rates studies (the probability of electron transfer is low so the time frame should be long), and to avoid any assumption on the electron transfer (such as suppressed for *z* above a given distance). As a matter of fact, currents as small as 100 fA can be generated with Q-biol. All numerical simulations presented in this study can be reproduced from the source code. **Q-biol code (v1 used in this study) will be made available open source at: https://github.com/QBIOL/qbiol.**

Main Assumptions and Simple Validations of the Code. Our code does not make any assumption such as a negligible electron transfer at a given distance *z* thanks to technical

computation implementations which improved the total computation time by orders of magnitude (see below), and inherently includes the tunnel resonant regime. The first assumption is that an average value of the electronic coupling (see below with Equation (12), (13)) has to be entered into the system. We simply adjust this value based on the experimental measurement of Figure 3. It can be compared with an independent measurement (Figure S12). The second assumption is that, to account for low reorganization energy observed for Fc-DNA attached on an electrode (Equation (14)),[32] we assume a small dielectric constant of 1.8 for water at the interface, which is anyway the value found experimentally for water in nanogaps.[34,35] This is useful for discussing the value of k_V (Figure S13). For simplicity in this study, we assume N = 1 (1 molecule) as all molecules are not correlated due to small enough surface density (we estimate a few tens molecules under the tip).

Electron Transfer Rates and Probabilities of Electron Transfer. We use the most general equations for Marcus electron transfer rates for oxidation (k_{ox}) and reduction (k_{red}) as a function of the Fc position z.

$$k_{ox}(z) = \frac{\rho H^2}{\hbar} e^{(-\beta_d z)} \sqrt{\frac{\pi}{\lambda(z) k_b T}} \int_{-\infty}^{+\infty} e^{\left(-\frac{(\varepsilon - E_f + V - \lambda(z))}{4\lambda(z) k_b T}\right)} \frac{1}{1 + e^{\left(\frac{\varepsilon - E_f}{k_b T}\right)}} d\varepsilon \qquad (12)$$

$$k_{red}(z) = \frac{\rho H^2}{\hbar} e^{(-\beta_d z)} \sqrt{\frac{\pi}{\lambda(z) k_b T}} \int_{-\infty}^{+\infty} e^{\left(-\frac{(\varepsilon - E_f - V - \lambda(z))}{4\lambda(z) k_b T}\right)} \frac{1}{1 + e^{\left(\frac{\varepsilon - E_f}{k_b T}\right)}} d\varepsilon \qquad (13)$$

where ρH^2 = 1.8×10^{-8} eV is the electronic coupling parameter at z = 0 that can be related to the standard electron transfer rate k_0 extracted experimentally, Figure S12. As mentioned above and in the paper, we consider that the electronic coupling is reduced by half in the case of dsDNA. β_d = 1 Å^{-1} is the tunnel decay ratio typically used[33] to account for the exponential decrease of the

electronic coupling with z; E_f = 0 vs Fc/Fc$^+$. The reorganization energy λ is also z-dependent (Equation (14)):

$$\lambda(z) = \frac{e^2}{(8\pi\varepsilon_0)}\left(\frac{1}{\varepsilon_{op}} - \frac{1}{\varepsilon_s}\right)\left(\frac{1}{a_0} - \frac{1}{[2(z+a_0)]}\right) \quad (14)$$

a_0 = 0.38 nm is the Fc radius. ε_{op} = 1.78 is the relative water permittivity at optical frequency, and ε_s = 1.8, the relative water permittivity of confined water. z is in fact (z + a_0) because our tracks start at z = 0 instead of a_0. Equation (14) is the typical equation used for λ. A small value for λ can also be confirmed experimentally from *I-V* curves at fixed z_{gap} (Figure S13) as in such a curve the current at half maximum is obtained at the reorganization energy. In contrast, in diffusion-limited processes, the curve shape is shifted to much larger voltages.

Equation (3) in the paper is simply derived starting from the assumption that the motion is so fast compared to electron transfer rates that the current can be described with the equation of a quantum dot (see for example the Supporting information of ref[37] for a detailed derivation). At $|V| >> k_BT$,

$$I = e\frac{\Gamma_b\Gamma_t}{\Gamma_b+\Gamma_t} \quad (15)$$

where Γ_b and Γ_t are the integrated electron transfer rates at the bottom and top electrodes, respectively. Taking into account the probabilities of presence at both interfaces as well as the tunnel decay ratio leads to Equation (3).

From Equation (12) and (13), probabilities of oxidation P_{ox} and reduction P_{red} in a time frame τ can be derived:

$$P_{ox} = 1\text{-}exp(-k_{ox} \cdot \tau) \quad (16)$$

$$P_{red} = 1\text{-}exp(-k_{red} \cdot \tau) \quad (17)$$

A table containing all values of k_{ox}, k_{red}, P_{ox}, P_{red} for z = 0 to 60 nm (step 0.01 nm) and the bias V is generated once and called during the computation as described below. This approach is very efficient computationally as integrals are not computed at each step, and even more importantly because parallel computation with the GPU can be performed from an array of values.

Technical Computation Details: Intuitive vs Rejection Sampling Approach

Two approaches can be used to perform such simulations. Both are based on probabilities of electron transfer at top and bottom surfaces, and the generation of random numbers to be compared with that leads to an eventual change of Fc charging state that reproduces the stochastic nature of the electron transfer process. The probabilities of electron transfer have been described above. We have implemented the rejection sampling approach which leads to gains by up to orders of magnitude in the simulation time on the tracks used. Our initial tests with the intuitive approach were too slow to have enough events for statistically representative current values or would have required several months for one bias condition.

Intuitive Approach. In the intuitive approach, we parse through the path data step by step, and we check whether an electron transfer occurs in an exact window of time (from time t to $t + \tau$, with dt step τ = 909 fs). This means that we always generate the same amount of random numbers and the same amount of comparisons of probabilities of electron transfer with random numbers, no matter what the electron transfer rates are.

Rejection Sampling Approach. In this approach, we estimate the waiting time until the next transition and Fc charging state. Results are strictly equivalent to the intuitive approach. However, it is much faster in terms of computation time, especially if waiting times correspond to thousands of dt steps. After each oxidation or reduction event, the time until the next transfer is simulated as

a Poissonian process with constant rate, equal to the maximum transfer rate (the value at $z = 0$). The proposed time is accepted with probability equal to the ratio between the instantaneous transfer rate at the current position, and the maximum rate used to simulate. In the rejection case, we can jump a lot of time steps without updating Fc charging state. This rejection sampling approach strongly depends on electron transfer rates. It is ideal for rates found in electrochemistry, but extremely long calculation times (hours) would have been observed if rates were multiplied by a factor of 1000, since the acceptance ratio would have been too small, and a majority of proposed events would have been rejected.

Technical computation details: Parallelization strategies (GPU)

The measured current is the average number of reduction events (Fc charging state changes) divided by the total track time. To get statistically representative currents, Q-biol performs Monte Carlo simulation using GPU parallel computation, with one GPU thread per MD track, on thousands of threads.

Fc-DNA synthesis and assembly

Oligonucleotides. Doubly HPLC purified, custom functionalized 20-mer and 35-mer oligonucleotides (oligo-dT), bearing a redox Fc label at their 3' end and a disulfide group at their 5' extremity, were from Eurogentec (Belgium). Their chemical structure was reported before.[32]

Preparation of Fc-ssDNA and Fc-dsDNA. The assembly of the Fc-DNA layer, and its hybridization were described elsewhere.[32]

Electrochemistry: Methods of Cyclic Voltammetry and AFM-SECM Experiments

The experimental details of cyclic voltammetry (CV) and AFM-SECM experiments have been reported before.[11,32,63] The AFM-SECM probes (tips), acting as combined microelectrodes and force sensors, were home-prepared from gold wires of 60 μm diameter as detailed previously.[64] These probes had a spring constant in the order of 1-5 nN/nm and a typical tip radius of ~100 nm. The interpretation of CV and AFM-SECM results are detailed in Supporting Discussion 5.

ASSOCIATED CONTENT

Supporting Information. The following files are available free of charge.

Supporting Discussion of the analysis of S_z using a numerical approach based on Kramers equations, S_z obtained from MD for dT_{20} and $(dT.dA)_{20}$ for various z_{gap} and peak splitting, analysis of $<\tau_{up}>$ and $<\tau_{down}>$, MD analysis for 35-mer DNA, interpretation of CV and AFM-SECM results, interpretation of k_0, ρH^2 and k_V, additional experiments with dT_{35} and $(dT.dA)_{35}$, supporting figures, and supporting table (PDF).

AUTHOR INFORMATION

Author Contributions

N.C., C. D. and A.F. obtained the funding, supervised the project and designed the experiments and simulations. I.M, C.G. and N.C. developed the Q-biol code the related analytical models and analyzed the related data. Z.Z conducted the CV and AFM-SECM experiments. A.C. and C.D. designed the AFM-SECM setup and initial experiments. A.F. performed simulations based on Kramers equations. S.G, S.L. K.N. and S.H.K provided continued insights on nanoelectrochemical results and Q-biol simulations. N.C. and C.D. co-wrote the paper with scientific interpretations and comments from all authors. λ: These authors equally contributed to the work.

Notes

The authors declare no competing financial interest.

ACKNOWLEDGMENT

The authors thank A. Bancaud, K. Hirakawa, S. Volz and R. Voituriez for discussions.

Funding: This work has received financial support from the French "Agence Nationale de la Recherche" (ANR) through the SIBI project (ANR-19-CE42-0011-01), the EU-ATTRACT (UNICORNDx) project and the BIOSTAT project from the Interdisciplinary research program at CNRS (MITI).

REFERENCES

(1) Li, T.; Kheifets, S.; Medellin, D.; Raizen, M. G. Measurement of the Instantaneous Velocity of a Brownian Particle. *Science* **2010**, *328*, 1673–1675.

(2) Huang, R.; Chavez, I.; Taute, K. M.; Lukić, B.; Jeney, S.; Raizen, M. G.; Florin, E. L. Direct Observation of the Full Transition from Ballistic to Diffusive Brownian Motion in a Liquid. *Nat. Phys.* **2011**, *7*, 576–580.

(3) Franosch, T.; Grimm, M.; Belushkin, M.; Mor, F. M.; Foffi, G.; Forró, L.; Jeney, S. Resonances Arising from Hydrodynamic Memory in Brownian Motion. *Nature* **2011**, *478*, 85–88.

(4) Li, T.; Raizen, M. G. Brownian Motion at Short Time Scales. *Ann. Phys.* **2013**, *525*, 281–295.

(5) Guérin, T.; Levernier, N.; Bénichou, O.; Voituriez, R. Mean First-Passage Times of Non-Markovian Random Walkers in Confinement. *Nature* **2016**, *534*, 356–359.

(6) Yang, H.; Luo, G.; Karnchanaphanurach, P.; Louie, T.-M.; Rech, I.; Cova, S.; Xun, L.; Xie, X. S. Protein Conformational Dynamics Probed by Single-Molecule Electron Transfer.

Science **2003**, *302*, 262–266.

(7) Kou, S. C.; Xie, X. S. Generalized Langevin Equation with Fractional Gaussian Noise: Subdiffusion within a Single Protein Molecule. *Phys. Rev. Lett.* **2004**, *93*, 1–4.

(8) Deutsch, J. M. Polymer Dynamics with Inertia. *J. Polym. Sci. Part B Polym. Phys.* **2012**, *50*, 379–386.

(9) Langer, A.; Kaiser, W.; Svejda, M.; Schwertler, P.; Rant, U. Molecular Dynamics of DNA-Protein Conjugates on Electrified Surfaces: Solutions to the Drift-Diffusion Equation. *J. Phys. Chem. B* **2014**, *118*, 597–607.

(10) Happel, J.; Brenner, H. Low Reynolds Number Hydrodynamics. In: *Mechanics of Fluids and Transport Processes*; Springer Netherlands: Dordrecht, 1983; pp 1–19.

(11) Wang, K.; Goyer, C.; Anne, A.; Demaille, C. Exploring the Motional Dynamics of End-Grafted DNA Oligonucleotides by in Situ Electrochemical Atomic Force Microscopy. *J. Phys. Chem. B* **2007**, *111*, 6051–6058.

(12) Armstrong, C. L.; Trapp, M.; Peters, J.; Seydel, T.; Rheinstädter, M. C. Short Range Ballistic Motion in Fluid Lipid Bilayers Studied by Quasi-Elastic Neutron Scattering. *Soft Matter* **2011**, *7*, 8358–8362.

(13) Levantino, M.; Schirò, G.; Lemke, H. T.; Cottone, G.; Glownia, J. M.; Zhu, D.; Chollet, M.; Ihee, H.; Cupane, A.; Cammarata, M. Ultrafast Myoglobin Structural Dynamics Observed with an X-Ray Free-Electron Laser. *Nat. Commun.* **2015**, *6*, 6772.

(14) Li, G.; Magana, D.; Dyer, R. B. Anisotropic Energy Flow and Allosteric Ligand Binding in Albumin. *Nat. Commun.* **2014**, *5*, 3100.

(15) Yuan, C.; Chen, H.; Lou, X. W.; Archer, L. A. DNA Bending Stiffness on Small Length Scales. *Phys. Rev. Lett.* **2008**, *100*, 1–4.

(16) Hogan, M. E.; Austin, R. H. Importance of DNA Stiffness in Protein-DNA Binding Specificity. *Nature* **1987**, *329*, 263–266.

(17) Mazur, A. K.; Maaloum, M. Atomic Force Microscopy Study of DNA Flexibility on Short Length Scales: Smooth Bending versus Kinking. *Nucleic Acids Res.* **2014**, *42*, 14006–14012.

(18) Kim, D.; Bowman, C.; Del Bonis-O'Donnell, J. T.; Matzavinos, A.; Stein, D. Giant Acceleration of DNA Diffusion in an Array of Entropic Barriers. *Phys. Rev. Lett.* **2017**, *118*, 1–5.

(19) Snodin, B. E. K.; Randisi, F.; Mosayebi, M.; Šulc, P.; Schreck, J. S.; Romano, F.; Ouldridge, T. E.; Tsukanov, R.; Nir, E.; Louis, A. A.; Doye, J. P. K. Introducing Improved Structural Properties and Salt Dependence into a Coarse-Grained Model of DNA. *J. Chem. Phys.* **2015**, *142*, 234901.

(20) Nomidis, S. K.; Kriegel, F.; Vanderlinden, W.; Lipfert, J.; Carlon, E. Twist-Bend Coupling and the Torsional Response of Double-Stranded DNA. *Phys. Rev. Lett.* **2017**, *118*, 1–6.

(21) Anne, A.; Demaille, C. Dynamics of Electron Transport by Elastic Bending of Short DNA Duplexes. Experimental Study and Quantitative Modeling of the Cyclic Voltammetric Behavior of 3′-Ferrocenyl DNA End-Grafted on Gold. *J. Am. Chem. Soc.* **2006**, *128*, 542–557.

(22) Anne, A.; Demaille, C. Electron Transport by Molecular Motion of Redox-DNA Strands: Unexpectedly Slow Rotational Dynamics of 20-Mer Ds-DNA Chains End-Grafted onto Surfaces via C6 Linkers. *J. Am. Chem. Soc.* **2008**, *130*, 9812–9823.

(23) Huang, K. C.; White, R. J. Random Walk on a Leash: A Simple Single-Molecule Diffusion Model for Surface-Tethered Redox Molecules with Flexible Linkers. *J. Am. Chem. Soc.* **2013**, *135*, 12808–12817.

(24) Dauphin-Ducharme, P.; Arroyo-Currás, N.; Adhikari, R.; Somerson, J.; Ortega, G.; Makarov, D. E.; Plaxco, K. W. Chain Dynamics Limit Electron Transfer from Electrode-Bound, Single-Stranded Oligonucleotides. *J. Phys. Chem. C* **2018**, *122*, 21441–21448.

(25) Reisner, W.; Morton, K. J.; Riehn, R.; Wang, Y. M.; Yu, Z.; Rosen, M.; Sturm, J. C.; Chou, S. Y.; Frey, E.; Austin, R. H. Statics and Dynamics of Single DNA Molecules Confined in

Nanochannels. *Phys. Rev. Lett.* **2005**, *94*, 1–4.

(26) *Main Page*. https://dna.physics.ox.ac.uk/index.php/Main_Page.

(27) de Gennes, P. G. Conformations of Polymers Attached to an Interface. *Macromolecules* **1980**, *13*, 1069–1075.

(28) Araújo, A.; Das, A. K.; Sousa, E. A Numerical Approach to Study the Kramers Equation for Finite Geometries: Boundary Conditions and Potential Fields. *J. Phys. A Math. Theor.* **2015**, *48*, 45202.

(29) Abbou, J.; Anne, A.; Demaille, C. Accessing the Dynamics of End-Grafted Flexible Polymer Chains by Atomic Force-Electrochemical Microscopy. Theoretical Modeling of the Approach Curves by the Elastic Bounded Diffusion Model and Monte Carlo Simulations. Evidence for Compression-Induced Late. *J. Phys. Chem. B* **2006**, *110*, 22664–22675.

(30) Yamahata, G.; Ryu, S.; Johnson, N.; Sim, H. S.; Fujiwara, A.; Kataoka, M. Picosecond Coherent Electron Motion in a Silicon Single-Electron Source. *Nat. Nanotechnol.* **2019**, *14*, 1019–1023.

(31) Q-Biol: GitHub (to Be Released at Paper Acceptance).

(32) Zheng, Z.; Kim, S. H.; Chovin, A.; Clement, N.; Demaille, C. Electrochemical Response of Surface-Attached Redox DNA Governed by Low Activation Energy Electron Transfer Kinetics. *Chem. Sci.* **2023**, *14*, 3652–3660.

(33) Trasobares, J.; Rech, J.; Jonckheere, T.; Martin, T.; Aleveque, O.; Levillain, E.; Diez-Cabanes, V.; Olivier, Y.; Cornil, J.; Nys, J. P.; Sivakumarasamy, R.; Smaali, K.; Leclere, P.; Fujiwara, A.; Théron, D.; Vuillaume, D.; Clément, N. Estimation of π-π Electronic Couplings from Current Measurements. *Nano Lett.* **2017**, *17*, 3215–3224.

(34) Fumagalli, L.; Esfandiar, A.; Fabregas, R.; Hu, S.; Ares, P.; Janardanan, A.; Yang, Q.; Radha, B.; Taniguchi, T.; Watanabe, K.; Gomila, G.; Novoselov, K. S.; Geim, A. K. Anomalously Low Dielectric Constant of Confined Water. *Science* **2018**, *360*, 1339–1342.

(35) Monet, G.; Berthoumieux, H.; Bresme, F.; Kornyshev, A. Nonlocal Dielectric Response of Water in Nanoconfinement. *Phys. Rev. Lett.* **2021**, *126*, 216001.

(36) Nitzan, A.; Galperin, M.; Ingold, G.-L.; Grabert, H. On the Electrostatic Potential Profile in Biased Molecular Wires. *J. Chem. Phys.* **2002**, *117*, 10837–10841.

(37) Garrigues, A. R.; Yuan, L.; Wang, L.; Mucciolo, E. R.; Thompon, D.; Del Barco, E.; Nijhuis, C. A. A Single-Level Tunnel Model to Account for Electrical Transport through Single Molecule-and Self-Assembled Monolayer-Based Junctions. *Sci. Rep.* **2016**, *6*, 1–15.

(38) Yuan, L.; Nerngchamnong, N.; Cao, L.; Hamoudi, H.; del Barco, E.; Roemer, M.; Sriramula, R. K.; Thompson, D.; Nijhuis, C. A. Controlling the Direction of Rectification in a Molecular Diode. *Nat. Commun.* **2015**, *6*, 6324.

(39) Davidchack, R. L.; Ouldridge, T. E.; Tretyakov, M. V. Geometric Integrator for Langevin Systems with Quaternion-Based Rotational Degrees of Freedom and Hydrodynamic Interactions. *J. Chem. Phys.* **2017**, *147*, 224103.

(40) Kim, B.; Hopcroft, M. A.; Candler, R. N.; Jha, C. M.; Agarwal, M.; Melamud, R.; Chandorkar, S. A.; Yama, G.; Kenny, T. W. Temperature Dependence of Quality Factor in MEMS Resonators. *J. Microelectromechanical Syst.* **2008**, *17*, 755–766.

(41) Lifshitz, R.; Roukes, M. Thermoelastic Damping in Micro- and Nanomechanical Systems. *Phys. Rev. B - Condens. Matter Mater. Phys.* **2000**, *61*, 5600–5609.

(42) Gil-Santos, E.; Baker, C.; Nguyen, D. T.; Hease, W.; Gomez, C.; Lemaître, A.; Ducci, S.; Leo, G.; Favero, I. High-Frequency Nano-Optomechanical Disk Resonators in Liquids. *Nat. Nanotechnol.* **2015**, *10*, 810–816.

(43) Velizhanin, K. A.; Chien, C. C.; Dubi, Y.; Zwolak, M. Driving Denaturation: Nanoscale Thermal Transport as a Probe of DNA Melting. *Phys. Rev. E - Stat. Nonlinear, Soft Matter Phys.* **2011**, *83*, 1–4.

(44) Sivakumarasamy, R.; Hartkamp, R.; Siboulet, B.; Dufrêche, J. F.; Nishiguchi, K.; Fujiwara, A.; Clément, N. Selective Layer-Free Blood Serum Ionogram Based on Ion-Specific

Interactions with a Nanotransistor. *Nat. Mater.* **2018**, *17*, 464–470.

(45) Li, Z.; Ruiz, V. G.; Kanduč, M.; Dzubiella, J. Ion-Specific Adsorption on Bare Gold (Au) Nanoparticles in Aqueous Solutions: Double-Layer Structure and Surface Potentials. *Langmuir* **2020**, *36*, 13457–13468.

(46) Steele, G. A.; Hüttel, A. K.; Witkamp, B.; Poot, M.; Meerwaldt, H. B.; Kouwenhoven, L. P.; Van Der Zant, H. S. J. Strong Coupling between Single-Electron Tunneling and Nanomechanical Motion. *Science* **2009**, *325*, 1103–1107.

(47) Chen, X.; Roemer, M.; Yuan, L.; Du, W.; Thompson, D.; Del Barco, E.; Nijhuis, C. A. Molecular Diodes with Rectification Ratios Exceeding 105 Driven by Electrostatic Interactions. *Nat. Nanotechnol.* **2017**, *12*, 797–803.

(48) Clement, N.; Fujiwara, A. Molecular Diodes: Breaking the Landauer Limit. *Nat. Nanotechnol.* **2017**, *12*, 725–726.

(49) Trasobares, J.; Vuillaume, D.; Théron, D.; Clément, N. A 17 GHz Molecular Rectifier. *Nat. Commun.* **2016**, *7*, 12850.

(50) Gustavsson, S.; Leturcq, R.; Simovič, B.; Schleser, R.; Ihn, T.; Studerus, P.; Ensslin, K.; Driscoll, D. C.; Gossard, A. C. Counting Statistics of Single Electron Transport in a Quantum Dot. *Phys. Rev. Lett.* **2006**, *96*, 76605.

(51) Grall, S.; Li, S.; Jalabert, L.; Kim, S.-H.; Chovin, A.; Demaille, C.; Clement, N. Electrochemical Shot-Noise of a Redox Monolayer. **2022**.

(52) Zevenbergen, M. A. G.; Singh, P. S.; Goluch, E. D.; Wolfrum, B. L.; Lemay, S. G. Stochastic Sensing of Single Molecules in a Nanofluidic Electrochemical Device. *Nano Lett.* **2011**, *11*, 2881–2886.

(53) Jonchhe, S.; Pandey, S.; Karna, D.; Pokhrel, P.; Cui, Y.; Mishra, S.; Sugiyama, H.; Endo, M.; Mao, H. Duplex DNA Is Weakened in Nanoconfinement. *J. Am. Chem. Soc.* **2020**, *142*, 10042–10049.

(54) Li, S.; Coffinier, Y.; Lagadec, C.; Cleri, F.; Nishiguchi, K.; Fujiwara, A.; Fujii, T.; Kim, S. H.; Clément, N. Redox-Labelled Electrochemical Aptasensors with Nanosupported Cancer Cells. *Biosens. Bioelectron.* **2022**, *216*, 114643.

(55) Cramer, P.; Bushnell, D. A.; Fu, J.; Gnatt, A. L.; Maier-Davis, B.; Thompson, N. E.; Burgess, R. R.; Edwards, A. M.; David, P. R.; Kornberg, R. D. Architecture of RNA Polymerase II and Implications for the Transcription Mechanism. *Science* **2000**, *288*, 640–649.

(56) Chen, W.-H.; Lu, G.; Bork, P.; Hu, S.; Lercher, M. J. Energy Efficiency Trade-Offs Drive Nucleotide Usage in Transcribed Regions. *Nat. Commun.* **2016**, *7*, 11334.

(57) Gibbons, A. The Calorie Counter. *Science* **2022**, *375*, 710–713.

(58) Ouldridge, T. E.; Louis, A. A.; Doye, J. P. K. Structural, Mechanical, and Thermodynamic Properties of a Coarse-Grained DNA Model. *J. Chem. Phys.* **2011**, *134*, 85101.

(59) Šulc, P.; Romano, F.; Ouldridge, T. E.; Rovigatti, L.; Doye, J. P. K.; Louis, A. A. Sequence-Dependent Thermodynamics of a Coarse-Grained DNA Model. *J. Chem. Phys.* **2012**, *137*, 135101.

(60) Uhlenbeck, G. E.; Ornstein, L. S. On the Theory of the Brownian Motion. *Phys. Rev.* **1930**, *36*, 823–841.

(61) Wang, M. C.; Uhlenbeck, G. E. On the Theory of the Brownian Motion II. *Rev. Mod. Phys.* **1945**, *17*, 323–342.

(62) Cutress, I. J.; Compton, R. G. How Many Molecules Are Required to Measure a Cyclic Voltammogram? *Chem. Phys. Lett.* **2011**, *508*, 306–313.

(63) Paiva, T. O.; Schneider, A.; Bataille, L.; Chovin, A.; Anne, A.; Michon, T.; Wege, C.; Demaille, C. Enzymatic Activity of Individual Bioelectrocatalytic Viral Nanoparticles: Dependence of Catalysis on the Viral Scaffold and Its Length. *Nanoscale* **2022**, *14*, 875–889.

(64) Abbou, J.; Demaille, C.; Druet, M.; Moiroux, J. Fabrication of Submicrometer-Sized Gold Electrodes of Controlled Geometry for Scanning Electrochemical-Atomic Force Microscopy. *Anal. Chem.* **2002**, *74*, 6355–6363.